THE JOURNAL OF PHYSICAL CHEMISTRY C

pubs.acs.org/JPCC Article

Electrochemical Deposition of Organometallic Halide Perovskite Single-Crystal Particles with Density Gradients and Their Stability, Fluorescence, and Photoelectrochemical Properties

Jeetika Yadav, Qiaoli Liang, and Shanlin Pan*

Cite This: J. Phys. Chem. C 2020, 124, 10659–10668 Read Online

ACCESS | Metrics & More | Article Recommendations | Supporting Information

ABSTRACT: Organometallic halide perovskites have gained immense scientific interest because of their unique optoelectronic properties that can benefit applications such as solar cells, lasers, and light-emitting diodes. Here, we develop a facile method to form a density gradient of $MAPbI_3$ (MA = methylammonium) crystal particles as a function of the electrochemical potential gradient across an indium-doped tin oxide (ITO) electrode. At the high-potential end of the ITO, a high density of nucleation sites is formed, yielding high-density $MAPbI_3$ crystals with a broad particle size distribution. Less density of $MAPbI_3$ crystals can be optically resolved at the low-potential end of the ITO. Spatial distributions of fluorescence and photoelectrochemical properties of the perovskite films show the same clear trends as the particle density gradients. Mass spectrum imaging of PbO_2 and $MAPbI_3$ gradients shows a spatial distribution of PbO_2, $MAPbI_3$ of fresh sample and PbI_2 for aged sample. Mass spectrum imaging also reveals a poor structural stability of $MAPbI_3$ crystals formed at the high-potential side of the gradient because of their fast growth kinetics producing smaller nucleation sites.

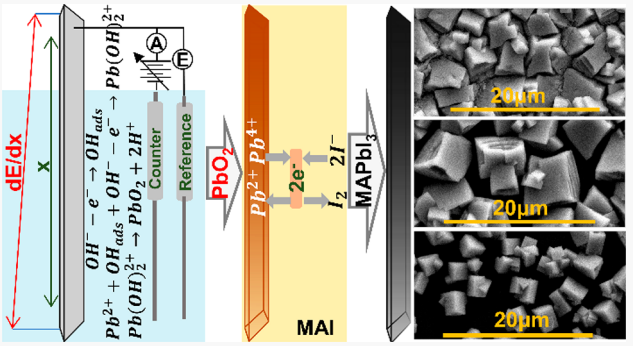

1. INTRODUCTION

Metal halide perovskites have general stoichiometry of ABX_3, where A and B are the cations and X is a halide.[1,2] A cations are usually large monovalent ions such as methylammonium $CH_3NH_3^+$ and formamidinium $(NH_2)_2CH^+$ and inorganic ions such as Cs^+, playing a crucial role in the stability of the perovskite structure.[3] B cations are the central ions such as Pb^{2+} crucial for tuning the band gap of the material.[4] The band gap of a metal halide perovskite can also be tuned by halide substitution. Usually the band gap increases if a lesser electronegative halide ion (X = I) is substituted with another more electronegative halide ion (X = Cl).[5,6] Owing to the unique properties such as broad spectra range,[7] intrinsic flexibility,[8] low cost,[8] direct band gap,[7] easy fabrication process,[8] long carrier lifetime, electrochemiluminescent properties, and high carrier mobility,[9] metal halide perovskites materials have been applied to various applications such as solar cells,[10−14] lasers,[15] and light-emitting diodes (LEDs).[8] The fabrication process for the LED based on single-crystal perovskite is challenging to scale up,[16] although epitaxial growth of the perovskite crystals has been reported.[17−19] For example, Hill et al.[19] introduced the electrochemical synthesis route to yield an epitaxial film of PbI_2 and subsequent conversion to $MAPbI_3$ perovskite with preferred [110] orientation. Koza and co-workers[18] introduced epitaxial film formation of $MAPbI_3$ through an electrochemical/chemical route on single-crystal Au substrates. Popov et al.[20] synthesized $MAPbI_3$ films by first electrodepositing PbO_2 films followed by two vapor conversion steps involving HI and CH_3NH_3I vapors. Lei et al.[17] synthesized single crystals of $MAPbBr_3$ with controlled morphology, locations, and orientations. Metallic Pb and Sn films can be transformed to halide perovskites using alcoholic solutions of methylammonium and formamidinium iodide.[21]

Intelligent surfaces coated with functional materials with gradients in surface coverage, porosity, particle size, and film thickness are highly attractive because of their potential applications in quantitative analysis applications and searching new catalysts. Various methods such as differential centrifugation,[22] potential gradient-driven electrodeposition,[23,24] and bipolar electrode[25] have been introduced to form functional on various substrates. For example, Jayaraman and co-workers[23] constructed a substrate possessing an electrocatalytic Pt gradient by applying a nonuniform electric field on the ITO surface. Subhramannia et al.[24] demonstrated a potential-

Received: February 21, 2020
Revised: April 19, 2020
Published: April 20, 2020

https://dx.doi.org/10.1021/acs.jpcc.0c01536
J. Phys. Chem. C 2020, 124, 10659−10668

dependent morphological evolution of Pt mesostructures by templated electrodeposition. Zhang et al. introduced a well-defined potential gradient for Au nanoparticles on the ITO surface.[26] Bipolar electrodes are used to create surface coverage gradients of self-assembled monolayers of small molecules[25] and DNA.[27]

Here, we report electrodeposition of $MAPbI_3$ perovskite crystal particles with their sizes and densities controlled by the electrochemical potential gradient of indium-doped tin oxide (ITO). To our knowledge, this is the first report demonstrating formation of a single-crystal particle density gradient of $MAPbI_3$ as a function of position potential on a single substrate. This facile electrodeposition method produces an ideal platform to efficiently search optimal electrodeposition conditions for well-defined single crystal particles that can be optically resolved and exhibit optical fluorescence and photoelectrochemical activities.

2. MATERIALS AND METHODS

2.1. Materials. All purchased chemicals were of reagent grade and used as received without further purification. $Pb(NO_3)_2$ (≥99.0%) was purchased from Sigma-Aldrich. NaOH and isopropanol were purchased from Alfa Aesar. CH_3NH_3I was synthesized according to previously reported literature.[28]

2.2. Synthesis of PbO_2 and $MAPbI_3$. PbO_2 was electrodeposited on 1.5 cm × 1.5 and 7.5 cm × 2.5 cm indium-doped tin oxide (ITO) with a sheet resistance of 30.8 Ω/□ substrate at 0.27, 0.3, 0.4, and 0.5 V for 254 s in 0.1 M $Pb(NO_3)_2$ in 5 M NaOH using Ag/AgCl and a graphite rod as the reference and counter electrodes, respectively.[18,29−31] The solution of 0.1 M $Pb(NO_3)_2$ in 5 M NaOH was prepared by dissolving lead nitrate in 5 M NaOH at 50 °C for 1 h under stirring. The subsequent conversion to $MAPbI_3$ was carried out by dipping the PbO_2 film in a 0.1 M CH_3NH_3I solution in isopropanol at 50 °C.

2.3. Mass Spectrometry and Other Characterization Methods. Matrix-assisted laser desorption ionization time of flight (MALDI-TOF) imaging mass spectrometry experiments were conducted on a Bruker Daltonics rapifleX mass spectrometer equipped with a smartbeam 3D laser ("Imaging 100 μm" as laser setup profile with raster width 200 μm). MALDI images were processed with FlexImaging 5.0 and SCiLS Lab software. FlexControl 4.0 software was used to examine the individual data point mass spectrum. X-ray diffraction (XRD) studies on the PbO_2 and $MAPbI_3$ gradients were performed using an X-ray diffractometer (Philips X'-Pert Pro X-ray, Cu Kα source). The surface morphology and the size distribution of the synthesized $MAPbI_3$ crystals were characterized using a JEOL 7000 scanning electron microscope (SEM). The PbO_2 film deposition was performed using a three-electrode configuration with an electrochemical workstation (CHI 760C, CH Instruments Inc., Austin, TX) using ITO, Ag/AgCl, and the graphite rod as the working, reference, and counter electrodes, respectively. The fluorescence spectra were collected by a CCD camera (Acton, SP2500 monochromator, Princeton Instruments) where the detector temperature was maintained at −100 °C with liquid nitrogen. The dark field, white field, and fluorescence images were collected by an electron-multiplying charge-coupled device, ANDOR technology iXON X3 EM-CCD camera using a 40× objective (NA = 0.75). Photoelectrochemical measurements were performed using a CHI760C biopotentiostat (CH Instruments Inc., Austin, TX) in a three-electrode configuration using ITO, Ag/AgCl, and a graphite rod as the working, reference, and counter electrodes, respectively. A standard simulated 1 sun (100 mW/cm^2) was provided by a solar simulator using a xenon lamp source (Oriel AM 1.5 filtered, Newport).

3. RESULTS AND DISCUSSION

3.1. Electrodeposition of PbO_2 and Chemical Transformation to $MAPbI_3$. Figure 1a shows the cyclic voltammetry (CV) experiments carried out in a three-electrode system for electrodeposition of PbO_2. The control experiments were performed without lead precursor ions to illustrate the electrodeposition location of the oxide film on ITO. The oxidation current of 1.1 mA observed at 0.47 V (vs Ag/AgCl) in the presence of $Pb(NO_3)_2$ confirms the oxidation and precipitation of Pb^{2+} ions. The oxidation peak at 0.47 V corresponds to the anodic deposition of PbO_2, whereas the irreversible cathodic peaks at 0.24, 0.93, and −0.07 V (vs Ag/AgCl) are associated with the reduction of $Pb(OH)_2^{2+}$, PbO_2, and reactive oxygen species produced by water oxidation. The mechanism for the PbO_2 electrodeposition is as follows[30−32]

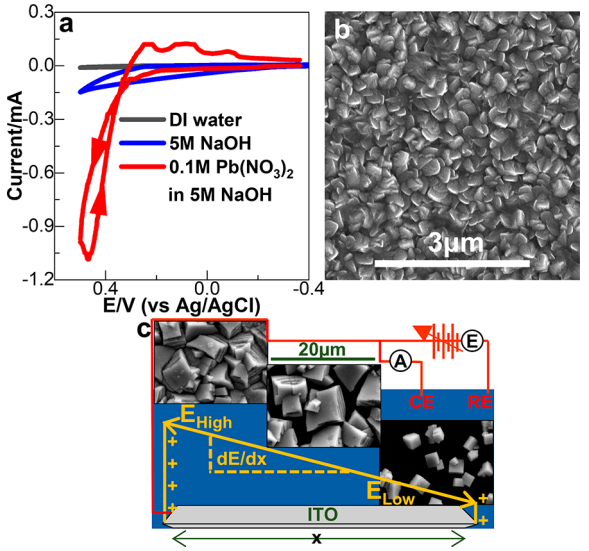

Figure 1. (a) CVs of the ITO electrode in the absence and presence of 0.1 M $Pb(NO_3)_2$ in 5 M NaOH for electrodeposition of PbO_2. (b) SEM image of PbO_2 electrodeposited at 0.3 V (vs Ag/AgCl) for 1 h using ITO (1.5 cm × 1.5 cm) as the working electrode, Ag/AgCl as the reference electrode, and graphite rod as the counter electrode. (c) Schematic representation of the potential gradient on 2.5 cm × 7.5 cm ITO. (Inset) Corresponding SEM images of $MAPbI_3$ (MA = methylammonium) crystals along the gradient.

$$OH^- - e^- \rightarrow OH_{ads} \quad (1)$$

$$Pb^{2+} + OH_{ads} + OH^- - e^- \rightarrow Pb(OH)_2^{2+} \quad (2)$$

$$Pb(OH)_2^{2+} \rightarrow PbO_2 + 2H^+ \quad (3)$$

Initially, the particles containing oxygen are chemisorbed on the electrode surface as OH_{ads} followed by electrochemical oxidation together with Pb^{2+} to form $Pb(OH)_2^{2+}$, which is deprotonated to yield PbO_2. The rate of the PbO_2 growth is dependent on the amount of intermediate product formed as shown in eq 2 at the electrode surface. The presence of these

https://dx.doi.org/10.1021/acs.jpcc.0c01536
J. Phys. Chem. C 2020, 124, 10659−10668

hydroxide complexes will be validated using the mass spectrum method at the end of the discussion.

After the initial CV study, anodic potentials of 0.24, 0.27, 0.30, 0.40, and 0.50 V (vs Ag/AgCl) were chosen for potentiostatic growth of PbO_2 on ITO substrate. Figure 1b shows the SEM image of PbO_2 film on ITO for the PbO_2 film deposited at 0.3 V vs Ag/AgCl for 3600 s and shows spindle-shaped geometry. Figure 1c shows the schematic representation of the formation of $MAPbI_3$ gradient on a 75 mm long ITO with the high-potential end showing formation of closely spaced $MAPbI_3$ crystals and the low-potential end showing the $MAPbI_3$ crystals farther spaced. Figure S1 shows the potential applied at the top of the ITO and at the opposite end of the ITO labeled as E_{bottom} as a function of applied potential. As can be seen from Figure S1, there is ~100 mV difference of potential at the top and bottom end of the ITO resulting in a potential gradient across the 7.5 cm length of the ITO. The resistance for the length of 7 cm of the ITO is 76.3 Ω.

$MAPbI_3$ film was formed by dipping PbO_2 electrodeposited film in 0.1 M MAI (MA = methylammonium, CH_3NH_3) in an isopropanol solution at 50 °C. Pb^{4+} ions are strong oxidants to oxidize iodide ions from the MAI solution. Therefore, the redox reaction between PbO_2 and MAI produces PbI_2 then $MAPbI_3$ by following the reactions shown in eqs 4 and 5[34]

$$Pb^{4+} + 2I^- \rightarrow Pb^{2+} + I_2 \quad (4)$$

$$PbI_2 + CH_3NH_3I \rightarrow CH_3NH_3PbI_3 \quad (5)$$

The conversion process of PbO_2 to $MAPbI_3$ was monitored by the variation of the electrode's open-circuit potential (OCP) using a Pt quasi-reference electrode (QRE) as shown in Figure S2.[18,33] The OCP value increases for the first 500 s due to dissolution of PbO_2 and formation of $MAPbI_3$, followed by a gradual decrease, suggesting complete conversion of PbO_2 to $MAPbI_3$ and reorganization of the perovskite film for single crystal particle formation.

3.2. PbO_2 and $MAPbI_3$ Gradient Formation on ITO Electrode. The PbO_2 gradient was induced on ITO (75 mm × 25 mm) substrate and subsequently converted to $MAPbI_3$. The top contact of the working electrode was made on the ITO with a Cu tape. To develop the gradient along the length of the ITO, 0.3 V (vs Ag/AgCl) was applied at the one end of the ITO attached to the Cu tape, keeping the ITO substrate stable in the electrolyte. The potential (E_x) along the length (L) of the ITO (gradient) at any location x can be determined with the linear eq 6 from an initial applied potential E_{appl} to the top of the ITO electrode

$$E_x = E_{appl} - \frac{x \times (E_{appl} - E_{bottom})}{L} \quad (6)$$

where E_{bottom} is the potential at the bottom end of the ITO electrode without direct electrical contact with the potentiostat. A film thickness gradient of PbO_2 is electrodeposited onto the ITO electrode at 0.3 V (vs Ag/AgCl) for 254 s (Figure 2a and 2b). The PbO_2 gradient formed at 0.3 V vs Ag/AgCl for 254 s is then converted to the $MAPbI_3$ gradient by dipping the film in 0.1 M MAI solution in isopropanol at 50 °C for 600 s. The appearance of the PbO_2 film changes from dark red to black during conversion as shown in the inset of Figure 2a. After complete conversion, there is no further change in the color of the film. The PbO_2 gradient provides control over the $MAPbI_3$ nucleation density and acts as a platform for tuning the mass transfer of lead ions reacting with MAI to form

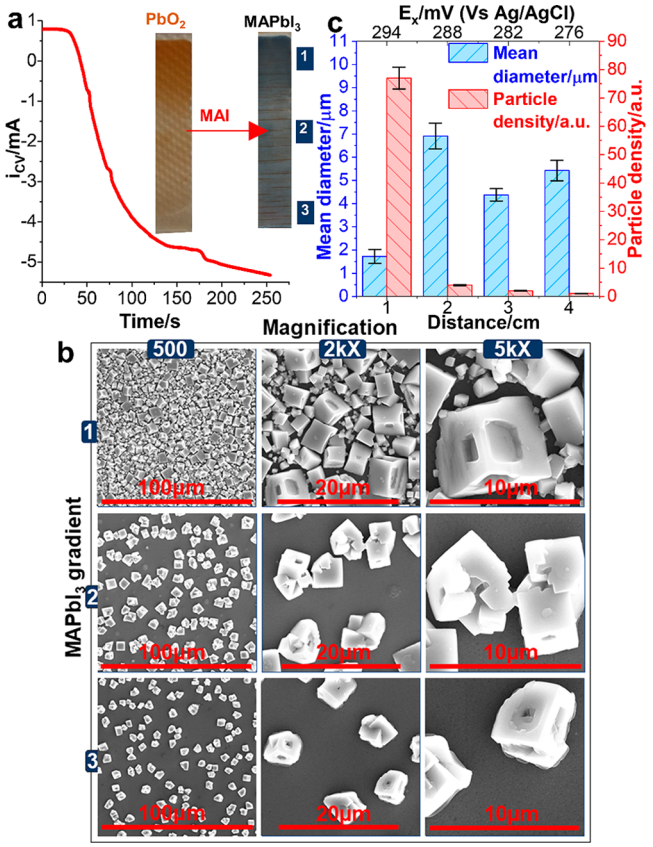

Figure 2. (a) Deposition of PbO_2 at 0.3 V for 254 s in 5 M NaOH, 0.1 M $Pb(NO_3)_2$ in 5 M NaOH using ITO (75 mm × 25 mm) as the working electrode, Ag/AgCl as the reference electrode, and graphite electrode as the counter electrode. (Inset) Electrodeposited gradient of PbO_2 and conversion of PbO_2 to $CH_3NH_3PbI_3$ by dipping PbO_2 in 0.1 M MAI solution in isopropanol at 50 °C for 600 s. $MAPbI_3$ gradient is labeled as 1, 2, and 3, showing the spots where SEM images are collected. (b) SEM images of $MAPbI_3$ gradient at magnifications of 500×, 2000×, and 5000× collected at spots 1 (top), 2 (middle), and 3 (bottom), where 1 corresponds to the high-potential end and 3 corresponds to the low-potential end of the ITO. (c) Average particle diameter and density dependences on the substrate location calculated by considering crystals as spheres. Error bars are shown for the mean particle size diameter calculated using the 95% confidence level.

crystals at the nucleation sites. The low-potential end with the thin PbO_2 film will form less nucleation sites to form monodispersed crystals. The thick oxide film at the high-potential end of the ITO provides high-density nucleation sites to form highly packed perovskite crystals with a broad crystal size distribution. The morphology of the produced $MAPbI_3$ gradient was investigated using scanning electron microscopy (SEM) and shows the crystal-like morphology. Previous studies have demonstrated formation of the $MAPbI_3$ crystal morphology on single-crystal Au substrate.[18,19] In this study, the perovskite crystals are formed on ITO as the gradient, suggesting that perovskite crystal formation strongly depends on the dissolution process of PbO_2 and mass transfer of MAI and lead ions. Figure 2b shows SEM images of perovskite crystals taken from the positions labeled 1, 2, and 3 in Figure 2a, where spot 1 corresponds to the high-potential end and spot 3 corresponds to the low-potential end of the perovskite gradient. As the photographed positions move toward the low-potential end, the $MAPbI_3$ crystals are farther spaced from

https://dx.doi.org/10.1021/acs.jpcc.0c01536
J. Phys. Chem. C 2020, 124, 10659−10668

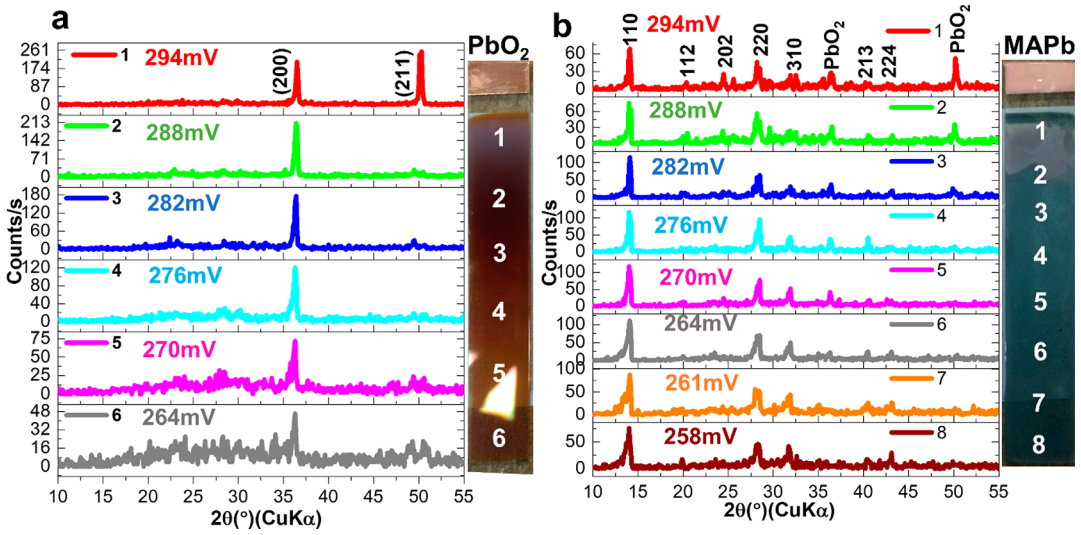

Figure 3. XRD of (a) PbO_2 gradient electrodeposited at 0.3 V for 254 s in 5 M NaOH, 0.1 M $Pb(NO_3)_2$ in 5 M NaOH using ITO (75 mm × 25 mm) as the working electrode, Ag/AgCl as the reference electrode, and graphite electrode as the counter electrode and (b) $MAPbI_3$ film formed by dipping PbO_2 in 0.1 M MAI solution in isopropanol at 50 °C for 600 s. PbO_2 and $MAPbI_3$ gradients are shown.

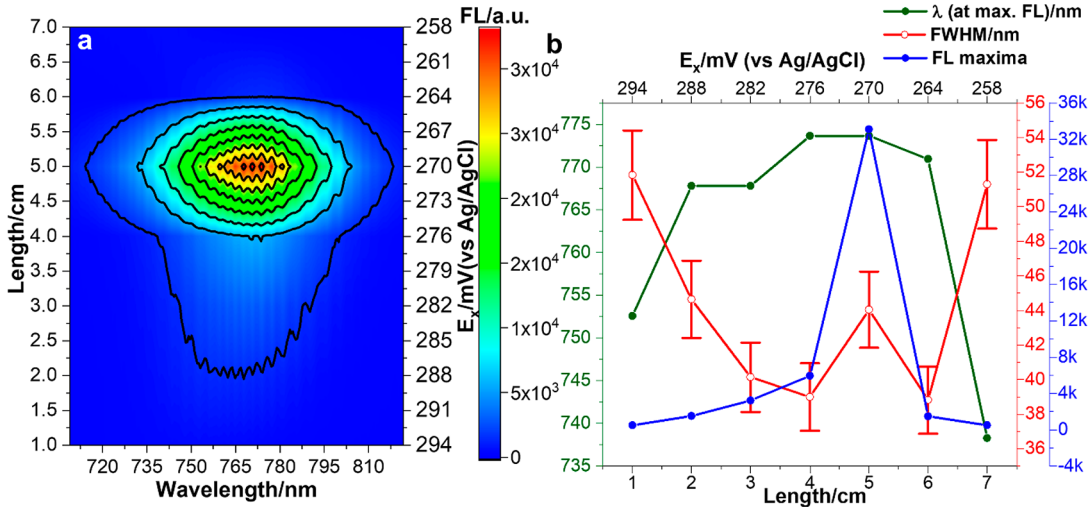

Figure 4. (a) Fluorescence spectrum (FL) dependency on the substrate location and corresponding electrochemical potential spatial distribution for PbO_2 deposition prior to being converted to $MAPbI_3$ when the ITO electrode was held at 0.3 V (vs Ag/AgCl). (b) Corresponding change in the maximum fluorescence intensity, full width at half maxima (FWHM), and shift in wavelength at maximum fluorescence intensity. Excitation wavelength is 532 nm.

each other. The yield of the crystals along the length of the gradient is calculated using the appearance ratio in the SEM images, and results are shown in Figure 2c. The particle shape evolution is accompanied by the coverage decrease throughout the length of the ITO (Figure 2b and 2c). The diameter of the crystals is increased initially, followed by a decrease in the diameter of the crystals considering crystals as spheres. The mean particle size of the $MAPbI_3$ crystals corresponding to 1, 2, 3, and 4 cm lengths of the ITO are 1.7 ± 0.30, 6.9 ± 0.55, 4.3 ± 0.26, and 5.4 ± 0.44 μm, respectively. The observed nonuniform trend in the mean diameter of the crystals is due to formation of varying sized crystals at the high-potential end of the electrode. The high-potential end of the ITO substrate results in anisotropic growth of $MAPbI_3$ crystals. The size distribution of the $MAPbI_3$ crystals is broad at the high-potential end due to the high nucleation seed density. The isotropy in morphology and crystal size increases as the lower potential end of the ITO is reached. The $MAPbI_3$ crystals are observed throughout the length of the ITO, depicting that the potentials (E_x) at all of the regions of the ITO are optimum for Pb^{2+} oxidation. SEM images clearly show that the substrate potential plays a critical role in controlling the $MAPbI_3$ crystal size isotropy and density, and the increase of the potential causes a steep increase in the surface coverage of $MAPbI_3$ crystals. Perovskite particle gradient can also form by pulling a PbO_2 substrate out of a MAI solution at a rate of 0.01 cm/s with a dipping machine as shown in Figure S3 (Supporting Information). Similar observations to 0.3 V are made when PbO_2 is electrodeposited at 0.5 V and consequently converted to $CH_3NH_3PbI_3$ (Figures S4 and S5, Supporting Information). The EDS (energy-dispersive X-ray spectroscopy) of the $MAPbI_3$ spectra is shown in Figure S6 (Supporting Information).

3.3. Structural and Optical Properties of $MAPbI_3$ Particle Density Gradient. The PbO_2 gradient obtained at 0.3 V (vs Ag/AgCl) for 254 s on ITO substrate (75 mm × 25

https://dx.doi.org/10.1021/acs.jpcc.0c01536
J. Phys. Chem. C 2020, 124, 10659−10668

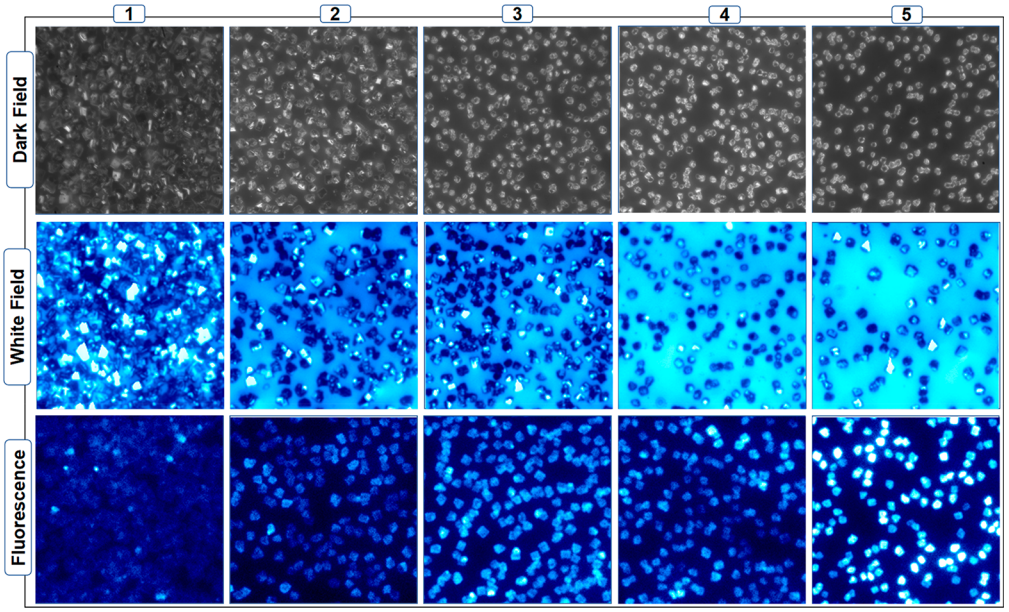

Figure 5. Dark field scattering, white field, and fluorescence images collected at different locations on the $MAPbI_3$ gradient. Film deposition conditions are located in the figure caption of Figure 3. Spot 1 corresponds to the high-potential end, and spot 5 corresponds to the low-potential end of the ITO shown in Figure 3.

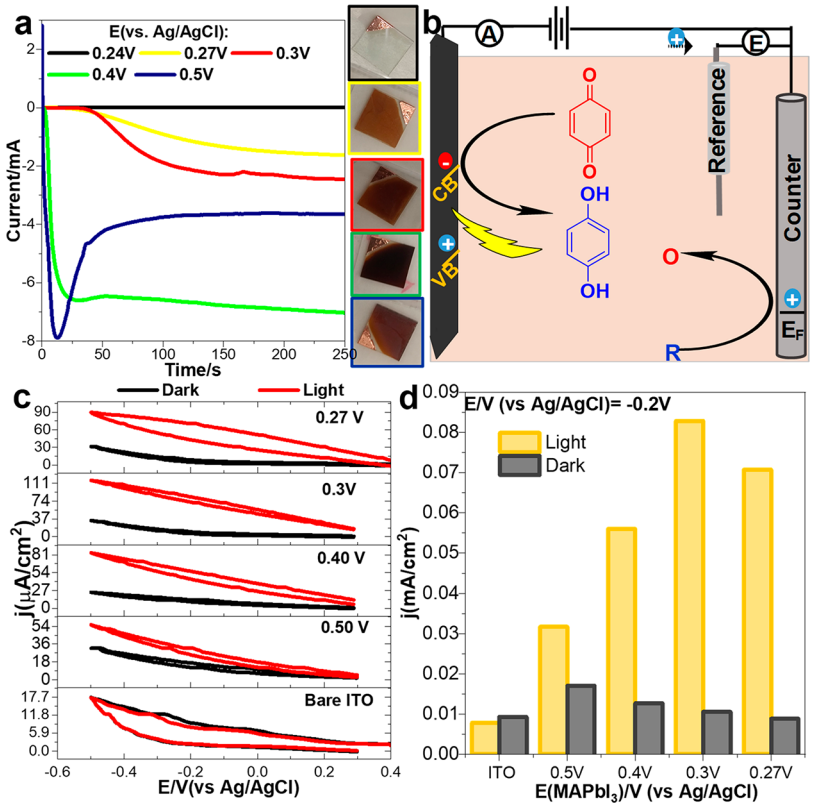

Figure 6. (a) PbO_2 electrodeposition at different potentials 0.24, 0.27, 0.3, 0.4, and 0.5 V in 0.1 M $Pb(NO_3)_2$ at an ITO (1.5 cm × 1.5 cm) working electrode, Ag/AgCl as the reference electrode, and graphite electrode as the counter electrode. Corresponding PbO_2 images are shown. (b) Schematic for photoelectrochemical measurement of benzoquinone reduction using $MAPbI_3$ as the photocathode under front illumination. (c) Photoelectrochemical measurements on 2 mM benzoquinone in 0.1 M $TBAPF_6$ in CH_2Cl_2 for $MAPbI_3$ films deposited at different potentials. (d) Bar graph representation of the photocurrent density measured at −0.2 V vs Ag/AgCl for $MAPbI_3$ films formed at different PbO_2 electrodeposition potentials.

mm) and the corresponding $MAPbI_3$ gradient were characterized by X-ray diffraction (XRD) to reveal their crystal structures and chemical identities. Figures 3a and S7a show the XRD patterns for the PbO_2 gradient at various locations labeled from 1 to 6, where location 1 indicates the high-potential end and location 6 indicates the low-potential end of

https://dx.doi.org/10.1021/acs.jpcc.0c01536
J. Phys. Chem. C 2020, 124, 10659−10668

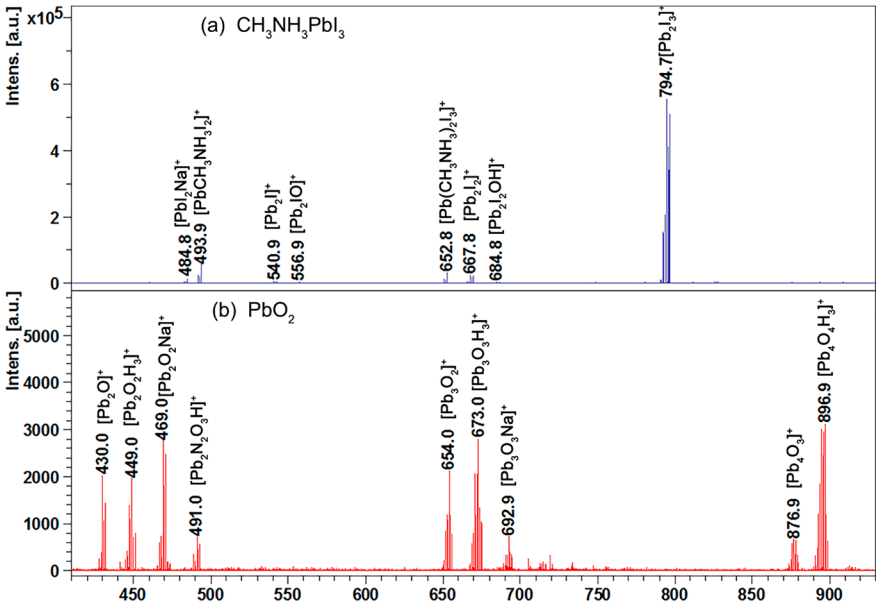

Figure 7. Selected mass spectrum assignment for m/z 400−900 for (a) $MAPbI_3$ and (b) PbO_2 films.

the ITO electrode. The two distinct phase peaks for β-PbO_2 are observed at the high-potential end of the ITO (location 1, Figure 3a, inset) corresponding to a 2θ of 36.1° (200) and 50° (211) with a preferred orientation of ß (211). In the low-potential end of the ITO, the peak indexed to the plane of ß (200) becomes pronounced (location 6, Figure 4a, inset), strongly suggesting that electrodeposited PbO_2 has various crystallographic orientations as a function of applied potential. Figures 3b and S7b (Supporting Information) show the XRD diffraction peaks[35,36] for the $MAPbI_3$ gradient. The diffraction peaks observed at 2θ = 14.02°, 20.0°, 24.6°, 28.36°, 31.76°, 40.47°, and 43.0° can be indexed to the (110), (112), (202), (220), (310), (213), and (224) planes, respectively. The diffraction peaks from the unreacted PbO_2 are also observed in the high-potential end of the ITO substrate (location 1, Figure 3b, inset). According to Debye Scherrer's formula, the calculated average crystallite sizes are 17.0, 89.0, 279.9, 114.0, 71.6, 14.5, 11.3, and 13.1 nm corresponding to the locations of 1, 2, 3, 4, 5, 6, 7, and 8 as shown in Figures 3b and S8 (Supporting Information). The crystallite size increases initially at the high-potential end and decreases at the low-potential end. A similar trend was observed in the SEM images in Figure 2c.

Figure 4a shows the fluorescence intensity contour plot as a function of wavelength and the applied potential under 532 nm laser excitation. The length of the ITO corresponding to 1 cm denotes the high-potential end, and the length of 7 cm corresponds to the low-potential end. Figure 4b shows the change in the fluorescence intensity along with the shift in the wavelength at maximum fluorescence intensity and the corresponding full width at half maxima (FWHM). The maximum fluorescence intensity for the $MAPbI_3$ gradient deposited at 300 mV (vs Ag/AgCl) is observed at 270 mV vs Ag/AgCl, and the wavelength is red shifted at this potential from 752.6 to 773.8 nm, suggesting quality formation of a large perovskite crystal with less defects than 300 mV (vs Ag/AgCl). The decrease in fluorescence from perovskite near the bottom of the ITO has to do with the surface coverage decrease of the crystal particles density per geometric surface area (Figure 2c). The FWHM decreases from 300 to 270 mV and increases after 270 mV (vs Ag/AgCl).

One of the benefits with well-dispersed single-crystal particles is that the optical and electrochemical properties of single entities can be studied as we demonstrated in our previously published work regarding local redox reactions at a single-nanoparticle level.[37−41] Figure 5 shows the dark field, white field, and the fluorescence images of single $MAPbI_3$ particles from the high-potential end of the ITO labeled as 1 to the lower potential end labeled as 5. The $MAPbI_3$ crystal density decreases from the high-potential end to the low-potential end similar to the observation in the SEM images (Figure 2b). Consistent with the fluorescence spectrum in Figure 4a, fluorescence images of single perovskite particles show an increase in the fluorescence intensity toward the low-potential end of ITO when the entire sample is under the same excitation intensity. There is no decrease in the fluorescence intensity of single-crystal particles from spot 3 to spot 5, although the average fluorescence spectrum intensity decreases in this region (Figure 4) because of the decrease in particle density per geometric surface area (Figure 2C).

3.4. Photoelectrochemical Properties of $MAPbI_3$ Films. PbO_2 films were deposited at potentials of 0.27, 0.3, 0.4, and 0.5 V (vs Ag/AgCl) for 254 s (Figure 6a) and transformed to $MAPbI_3$ by dipping PbO_2 films in 0.1 M MAI in isopropanol for 600 s. PbO_2 is a highly conductive oxide; hence, the increase in the current is associated with the increase in PbO_2 thickness on the ITO substrate. The $i-t$ curves of >0.4 V deposition show an initial sharp increase due to nucleation site development on ITO, followed by a decrease in current due to the mass transfer limitation of lead ions, and then a slow increase to a plateau of a steady-state value for crystal size increase.[32,42] As shown in Figure 6a, all of the substrates were deposited for 254 s at 0.24, 0.27, 0.30, 0.40, and 0.50 V. The corresponding images of the electrodeposited film of PbO_2 at different potentials are shown in Figure 6a. The color of the electrodeposited PbO_2 films changes from brown to dark red with an increase in film thickness. The photoelectrochemical performance of the synthesized

https://dx.doi.org/10.1021/acs.jpcc.0c01536
J. Phys. Chem. C 2020, 124, 10659−10668

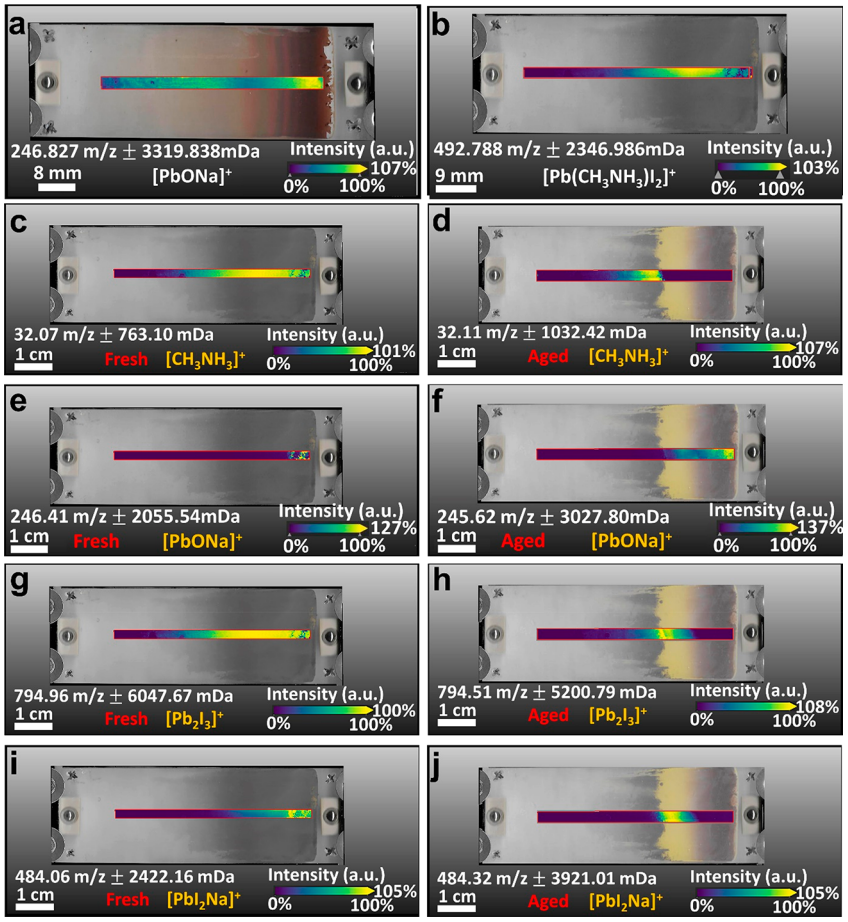

Figure 8. Mass spectrum (MS) imaging of (a) PbO_2 and (b) $MAPbI_3$ gradients. Stability study of $MAPbI_3$ gradients using the MS imaging technique for the fresh (c, e, g, and i) and aged (d, f, h, and j) gradients for $[CH_3NH_3]^+$, $[PbONa]^+$, $[Pb_2I_3]^+$, and $[PbI_2Na]^+$ fragments, respectively.

$MAPbI_3$ films by electrodeposition/chemical conversion at different potentials was studied.

Figure 6b shows the schematic for the photoelectrochemical study using $MAPbI_3$ films as the photocathode. The $MAPbI_3$ films deposited at different potentials are utilized as the photocathode working electrode with a graphite rod as the counter electrode and Ag/AgCl as the reference electrode. The cathodic photocurrent is produced upon illumination to reduce *p*-benzoquinone (BQ) to hydroquinone (HQ) at the working electrode.[43] Figure 6c shows that the electrodeposited $MAPbI_3$ has a small amount of dark current, suggesting that the ITO surface is not protected with $MAPbI_3$ films. Upon illumination, an enhancement of the photocurrent for the *p*-benzoquinone reduction is observed and increases with the applied potential. A bar graph at −0.2 V vs Ag/AgCl is plotted in Figure 6d to illustrate a deposition potential effect on photoelectrochemical current density under light and dark conditions. $MAPbI_3$ film deposited at 0.3 V has a photoelectrochemical current of 0.083 mA/cm^2 at −0.2 V (vs Ag/AgCl) as compared to the photocurrent density of 0.070, 0.055, and 0.032 mA/cm^2 for the $MAPbI_3$ films synthesized at 0.27, 0.4, and 0.5 V, respectively, because of the optimum crystallinity of the film and minimum loss of the photogenerated charge carriers at 0.3 V vs Ag/AgCl. The maximum dark current density of 0.017 mA/cm^2 at −0.2 V is observed for the $MAPbI_3$ film deposited at 0.5 V, whereas for the $MAPbI_3$ films deposited at 0.4, 0.3, and 0.27 V correspond to dark current densities of 0.013, 0.010, and 0.009 mA/cm^2 respectively. The photoelectrochemical performance can be further improved by controlling the film thickness, crystal size, and particle density to maximize photoelectrochemical photocurrent while minimizing the dark current.

3.5. Mass Spectrometry of the $MAPbI_3$ Gradient. To resolve the chemical identity and stability of the electrodeposited perovskite product, the spatial chemical distribution of the perovskite crystal gradients are measured with the matrix-assisted laser desorption ionization-time-of-flight (MALDI-TOF) imaging technique. Figure 7 shows the MS analysis[44] of the PbO_2 (Figure 7a) and $MAPbI_3$ (Figure 7b) gradients cast on the MALDI imaging ITO slide with peak assignments. The MS spectra of PbO_2 shown in Figure 7a show a mixture of $Pb(OH)_2^{2+}$ and PbO_2 on the PbO_2 gradient, indicating that the excess MA ions produced by reactions 4 and 5 can be neutralized by residual OH ions during the oxide-to-perovskite transformation process.

The MALDI imaging technique was used to study the chemical composition of $MAPbI_3$ and PbO_2 gradients cast on the ITO slide by overlaying MS images at selected m/z with the ITO slide visual images. Figure 8a and 8b shows the MS image of the PbO_2 gradient for the $[PbONa]^+$ fragment corresponding to m/z 246.827 ± 3319.838 mDa, and Figure 8b shows the MS image of the $CH_3NH_3PbI_3$ gradient for the $[Pb(CH_3NH_3)I_2]^+$ fragment corresponding to m/z 492.788 ± 2346.986 mDa. The intensity of the selected fragments

https://dx.doi.org/10.1021/acs.jpcc.0c01536
J. Phys. Chem. C 2020, 124, 10659−10668

increases at the high-potential end of the ITO and decreases at the low-potential end of the ITO. These observations are consistent with the SEM images shown in Figure 2b, suggesting that deposition of the film at the high-potential end of the ITO is more abundant as compared to the low-potential end of the ITO. The MS imaging technique was also used to identify the trend of various fragments for the fresh (Figure 8c, 8e, 8g, and 8i) versus the aged (Figure 8d, 8f, 8h, and 8j) $MAPbI_3$ gradient. Figure 8c and 8d shows the $MAPbI_3$ gradient MS images for the $[CH_3NH_3]^+$ fragment corresponding m/z to 32.1. The fresh sample shows the high intensity of the $[CH_3NH_3]^+$ fragment at the high-potential end, whereas for the aged sample the intensity for the $[CH_3NH_3]^+$ fragment is decreased at the high-potential end, suggesting loss of $[CH_3NH_3]^+$ over time starting at the high-potential end, which correlates well with the visual ITO image color change (black to bright yellow). Figure 8e and 8f shows the MS images for the $[PbONa]^+$ fragment for the fresh and aged $MAPbI_3$ gradient, respectively. The peak intensity of the $[PbONa]^+$ fragment is negligible at the fresh $MAPbI_3$ gradient and increases in intensity as the gradient is aged (Figure 8f), suggesting that once the $[CH_3NH_3]^+$ cation is lost over time the perovskite structure is degraded and the unreacted PbO_2 generated a $[PbONa]^+$ fragment for the aged sample. Figure 8g and 8i shows MS images of the $MAPbI_3$ fresh gradient for the $[Pb_2I_3]^+$ and $[PbI_2Na]^+$ fragments, respectively. Their corresponding MS images for the aged gradients are shown in Figure 8h and 8j, respectively, showing weaker intensity than the fresh samples due to loss of the perovskite structure.

The XRD in Figure 3b shows some of the unreacted PbO_2 at the high-potential end of the $MAPbI_3$ gradient, which is consistent with MS imaging analysis (Figure 8e and 8f). At the high-potential end of the ITO there are high-density nucleation sites for MAI to react with PbO_2 and some of the PbO_2 remains unreacted. The increase in intensity for the $[PbONa]^+$ fragment as well as the decrease in the intensity for the $[CH_3NH_3]^+$ fragment, for the aged gradient at the high-potential end, demonstrates the loss of the perovskite structure at the high-potential end. The stability of the $MAPbI_3$ gradient is poor at the high-potential end due to the fast growth of $MAPbI_3$ crystals with varying sizes at the high nucleation sites region along with unreacted PbO_2 and the loss of MA^+. In accordance with this observation, the fluorescence of the $MAPbI_3$ crystals is low at the high-potential end and high at the low-potential end while attaining maximum fluorescence intensity for the 270 mV for the gradient formed at 300 mV (vs Ag/AgCl), shown in Figures 4a, 4b, and 5. As shown in Figure 6c and 6d, the maximum photoelectrochemical photocurrent density of 0.083 mA/cm^2 is observed for $MAPbI_3$ film deposited at 0.3 V as compared to films deposited at 0.5, 0.4, and 0.27 V vs Ag/AgCl. This suggests that there is an optimum potential with the minimum defect sites and maximum coverage to prevent the loss of photogenerated charge carriers in photoelectrochemical measurements. The high-potential end of the $MAPbI_3$ gradient is comprised of the trap sites for quenching the photogenerated charge carriers in the PEC photoelectrochemical measurements. The article density and size distribution are uneven at the high-potential end of the ITO and uniform at the low-potential end of the ITO as shown in Figure 2b, which corresponds to the instability at the high-potential end as shown in the MS images in Figure 8c, 8d, 8e, and 8f.

4. CONCLUSIONS

In summary, single-crystal $MAPbI_3$ particles can be electrodeposited onto a single ITO substrate. The electrochemical potential gradient of the ITO electrode controls the $MAPbI_3$ crystal size and density. The high-potential end of the ITO has high nucleation sites and shows formation of a high-density $MAPbI_3$ crystal. The low-potential end of the ITO shows the spatially distributed micrometer-sized crystals. Crystal particles deposited at a potential of less than 270 mV (vs Ag/AgCl) show enhanced fluorescence and photoelectrochemical performance than the high electrode potential side of the gradient. Mass spectrometry imaging study confirms the initial gradients of PbO_2 and $MAPbI_3$ in fresh sample and PbI_2 in the aged sample upon loss of methylammonium. Mass spectrometry analysis shows an increase in the intensity of $[PbONa]^+$ at the high-potential end of the gradient and decrease in intensity of the $[CH_3NH_3]^+$ fragment as the sample is aged due to loss of the perovskite structure. The spatial distributions of $[CH_3NH_3]^+$ and $[PbONa]^+$ and other fragments are sensitive to the anisotropy of $MAPbI_3$ crystal sizes at the high-potential end. Mass spectrum imaging also reveals that the poor stability of the $MAPbI_3$ gradient is poor at the high-potential side with fast growth kinetics of $MAPbI_3$ crystals with smaller high-nucleation sites than the lower particle density side.

■ ASSOCIATED CONTENT

Supporting Information

The Supporting Information is available free of charge at https://pubs.acs.org/doi/10.1021/acs.jpcc.0c01536.

> Information about the $MAPbI_3$ crystals growth as a function of reaction time of PbO_2 with MAI, change in open-circuit potential as a function of reaction between MAI and PbO_2, and formation of $MAPbI_3$ gradient at 0.5 V (PDF)

■ AUTHOR INFORMATION

Corresponding Author

Shanlin Pan − *Department of Chemistry and Biochemistry, The University of Alabama, Tuscaloosa, Alabama 35487-0336, United States;* orcid.org/0000-0003-2226-9687; Email: span1@ua.edu

Authors

Jeetika Yadav − *Department of Chemistry and Biochemistry, The University of Alabama, Tuscaloosa, Alabama 35487-0336, United States*

Qiaoli Liang − *Department of Chemistry and Biochemistry, The University of Alabama, Tuscaloosa, Alabama 35487-0336, United States*

Complete contact information is available at: https://pubs.acs.org/10.1021/acs.jpcc.0c01536

Author Contributions

The manuscript was written through the contributions of all authors. All authors have given approval to the final version of the manuscript.

Notes

The authors declare no competing financial interest.

https://dx.doi.org/10.1021/acs.jpcc.0c01536
J. Phys. Chem. C 2020, 124, 10659−10668

■ ACKNOWLEDGMENTS

We are thankful for the financial support from the National Science Foundation (NSF award CHE 1508192 and OIA 1539035). We acknowledge the support of the grant NSF CHE-1726812 from the Major Research Instrumentation Program for the purchase of the MALDI/TOF-TOF mass spectrometer UA. We acknowledge support from the University of Alabama.

■ ABBREVIATIONS

MALDI-TOF, matrix-assisted laser desorption ionization time-of-flight; XRD, X-ray diffraction; BQ, benzoquinone; FWHM, full width at half maxima; MA, methylammonium

■ REFERENCES

(1) Jena, A. K.; Kulkarni, A.; Miyasaka, T. Halide Perovskite Photovoltaics: Background, Status, and Future Prospects. *Chem. Rev.* **2019**, *119*, 3036−3103.
(2) Shamsi, J.; Urban, A. S.; Imran, M.; De Trizio, L.; Manna, L. Metal Halide Perovskite Nanocrystals: Synthesis, Post-Synthesis Modifications, and Their Optical Properties. *Chem. Rev.* **2019**, *119*, 3296−3348.
(3) Amat, A.; Mosconi, E.; Ronca, E.; Quarti, C.; Umari, P.; Nazeeruddin, M. K.; Grätzel, M.; De Angelis, F. Cation-Induced Band-Gap Tuning in Organohalide Perovskites: Interplay of Spin−Orbit Coupling and Octahedra Tilting. *Nano Lett.* **2014**, *14*, 3608−3616.
(4) Yin, W.-J.; Shi, T.; Yan, Y. Unique Properties of Halide Perovskites as Possible Origins of the Superior Solar Cell Performance. *Adv. Mater.* **2014**, *26*, 4653−4658.
(5) Li, C.; Wei, J.; Sato, M.; Koike, H.; Xie, Z.-Z.; Li, Y.-Q.; Kanai, K.; Kera, S.; Ueno, N.; Tang, J.-X. Halide-Substituted Electronic Properties of Organometal Halide Perovskite Films: Direct and Inverse Photoemission Studies. *ACS Appl. Mater. Interfaces* **2016**, *8*, 11526−11531.
(6) Eperon, G. E.; Stranks, S. D.; Menelaou, C.; Johnston, M. B.; Herz, L. M.; Snaith, H. J. Formamidinium Lead Trihalide: a Broadly Tunable Perovskite for Efficient Planar Heterojunction Solar Cells. *Energy Environ. Sci.* **2014**, *7*, 982−988.
(7) Miyasaka, T. Perovskite Photovoltaics: Rare Functions of Organo Lead Halide in Solar Cells and Optoelectronic Devices. *Chem. Lett.* **2015**, *44*, 720−729.
(8) Kim, Y.-H.; Cho, H.; Heo, J. H.; Kim, T.-S.; Myoung, N.; Lee, C.-L.; Im, S. H.; Lee, T.-W. Multicolored Organic/Inorganic Hybrid Perovskite Light-Emitting Diodes. *Adv. Mater.* **2015**, *27*, 1248−1254.
(9) Noh, J. H.; Im, S. H.; Heo, J. H.; Mandal, T. N.; Seok, S. I. Chemical Management for Colorful, Efficient, and Stable Inorganic−Organic Hybrid Nanostructured Solar Cells. *Nano Lett.* **2013**, *13*, 1764−1769.
(10) Kojima, A.; Teshima, K.; Shirai, Y.; Miyasaka, T. Organometal Halide Perovskites as Visible-Light Sensitizers for Photovoltaic Cells. *J. Am. Chem. Soc.* **2009**, *131*, 6050−6051.
(11) Liu, M.; Johnston, M. B.; Snaith, H. J. Efficient Planar Heterojunction Perovskite Solar Cells by Vapour Deposition. *Nature* **2013**, *501*, 395−398.
(12) Jeon, N. J.; Noh, J. H.; Yang, W. S.; Kim, Y. C.; Ryu, S.; Seo, J.; Seok, S. I. Compositional Engineering of Perovskite Materials for High-Performance Solar Cells. *Nature* **2015**, *517*, 476−480.
(13) Ball, J. M.; Lee, M. M.; Hey, A.; Snaith, H. J. Low-Temperature Processed Meso-Superstructured to Thin-Film Perovskite Solar Cells. *Energy Environ. Sci.* **2013**, *6*, 1739−1743.
(14) Zhou, H.; Chen, Q.; Li, G.; Luo, S.; Song, T.-b.; Duan, H.-S.; Hong, Z.; You, J.; Liu, Y.; Yang, Y. Interface Engineering of Highly Efficient Perovskite Solar Cells. *Science* **2014**, *345*, 542−546.
(15) D'Innocenzo, V.; Srimath Kandada, A. R.; De Bastiani, M.; Gandini, M.; Petrozza, A. Tuning the Light Emission Properties by Band Gap Engineering in Hybrid Lead Halide Perovskite. *J. Am. Chem. Soc.* **2014**, *136*, 17730−17733.
(16) Chen, M.; Shan, X.; Geske, T.; Li, J.; Yu, Z. Manipulating Ion Migration for Highly Stable Light-Emitting Diodes with Single-Crystalline Organometal Halide Perovskite Microplatelets. *ACS Nano* **2017**, *11*, 6312−6318.
(17) Lei, Y.; Chen, Y.; Gu, Y.; Wang, C.; Huang, Z.; Qian, H.; Nie, J.; Hollett, G.; Choi, W.; Yu, Y.; et al. Controlled Homoepitaxial Growth of Hybrid Perovskites. *Adv. Mater.* **2018**, *30*, 1705992−1705999.
(18) Koza, J. A.; Hill, J. C.; Demster, A. C.; Switzer, J. A. Epitaxial Electrodeposition of Methylammonium Lead Iodide Perovskites. *Chem. Mater.* **2016**, *28*, 399−405.
(19) Hill, J. C.; Koza, J. A.; Switzer, J. A. Electrodeposition of Epitaxial Lead Iodide and Conversion to Textured Methylammonium Lead Iodide Perovskite. *ACS Appl. Mater. Interfaces* **2015**, *7*, 26012−26016.
(20) Popov, G.; Mattinen, M.; Kemell, M. L.; Ritala, M.; Leskela, M. Scalable Route to the Fabrication of $CH_3NH_3PbI_3$ Perovskite Thin Films by Electrodeposition and Vapor Conversion. *ACS Omega* **2016**, *1*, 1296−1306.
(21) Rakita, Y.; Gupta, S.; Cahen, D.; Hodes, G. Metal to Halide Perovskite (HaP): An Alternative Route to HaP Coating, Directly From Pb(0) or Sn(0) Films. *Chem. Mater.* **2017**, *29*, 8620−8629.
(22) Sun, X.; Tabakman, S. M.; Seo, W. S.; Zhang, L.; Zhang, G.; Sherlock, S.; Bai, L.; Dai, H. Separation of Nanoparticles in a Density Gradient: FeCo@C and Gold Nanocrystals. *Angew. Chem., Int. Ed.* **2009**, *48*, 939−942.
(23) Jayaraman, S.; Hillier, A. C. Construction and Reactivity Mapping of a Platinum Catalyst Gradient Using the Scanning Electrochemical Microscope. *Langmuir* **2001**, *17*, 7857−7864.
(24) Subhramannia, M.; Ramaiyan, K.; Pillai, V. K. Comparative Study of the Shape-Dependent Electrocatalytic Activity of Platinum Multipods, Discs, and Hexagons: Applications for Fuel Cells. *Langmuir* **2008**, *24*, 3576−3583.
(25) Ulrich, C.; Andersson, O.; Nyholm, L.; Björefors, F. Formation of Molecular Gradients on Bipolar Electrodes. *Angew. Chem., Int. Ed.* **2008**, *47*, 3034−3036.
(26) Zhang, D.; Diao, P.; Zhang, Q. Potential-Induced Shape Evolution of Gold Nanoparticles Prepared on ITO Substrate. *J. Phys. Chem. C* **2009**, *113*, 15796−15800.
(27) Chow, K.-F.; Mavré, F.; Crooks, R. M. Wireless Electrochemical DNA Microarray Sensor. *J. Am. Chem. Soc.* **2008**, *130*, 7544−7545.
(28) Im, J.-H.; Lee, C.-R.; Lee, J.-W.; Park, S.-W.; Park, N.-G. 6.5% Efficient Perovskite Quantum-Dot-Sensitized Solar Cell. *Nanoscale* **2011**, *3*, 4088−4093.
(29) Vertegel, A. A.; Bohannan, E. W.; Shumsky, M. G.; Switzer, J. A. Epitaxial Electrodeposition of Orthorhombic α PbO_2 on (100)-Oriented Single Crystal Au. *J. Electrochem. Soc.* **2001**, *148*, C253−C256.
(30) Lee, J.; Varela, H.; Uhm, S.; Tak, Y. Electrodeposition of PbO_2 onto Au and Ti Substrates. *Electrochem. Commun.* **2000**, *2*, 646−652.
(31) Velichenko, A. B.; Girenko, D. V.; Danilov, F. I. Mechanism of Lead Dioxide Electrodeposition. *J. Electroanal. Chem.* **1996**, *405*, 127−132.
(32) Velichenko, A. B.; Girenko, D. V.; Danilov, F. I. Electrodeposition of Lead Dioxide at an Au Electrode. *Electrochim. Acta* **1995**, *40*, 2803−2807.
(33) Seruga, M.; Hasenay, D. Electrochemical and Surface Properties of Aluminium in Citric Acid Solutions. *J. Appl. Electrochem.* **2001**, *31*, 961−967.
(34) Jain, S. M.; Philippe, B.; Johansson, E. M. J.; Park, B.-w.; Rensmo, H.; Edvinsson, T.; Boschloo, G. Vapor Phase Conversion of PbI_2 to $CH_3NH_3PbI_3$: Spectroscopic Evidence for Formation of an Intermediate Phase. *J. Mater. Chem. A* **2016**, *4*, 2630−2642.
(35) Fibriyanti, A. A.; Mufti, N.; Fuad, A.; Latifah, E.; Kurniawan, R.; Yogihati, C. I.; Hidayat, N. Improved Solar Cell and Photoresponse

https://dx.doi.org/10.1021/acs.jpcc.0c01536
J. Phys. Chem. C 2020, 124, 10659−10668

Performance of $CH_3NH_3PbI_3$ Perovskite With ZnO Nanorods. *IOP Conf. Ser.: Mater. Sci. Eng.* **2019**, *515*, 012089−012095.
(36) Zhang, C.; Luo, Y.; Chen, X.; Chen, Y.; Sun, Z.; Huang, S. Effective Improvement of the Photovoltaic Performance of Carbon-Based Perovskite Solar Cells by Additional Solvents. *Nano-Micro Lett.* **2016**, *8*, 347−357.
(37) Hill, C. M.; Pan, S. A Dark-Field Scattering Spectroelectrochemical Technique for Tracking the Electrodeposition of Single Silver Nanoparticles. *J. Am. Chem. Soc.* **2013**, *135*, 17250−17253.
(38) Hill, C. M.; Bennett, R.; Zhou, C.; Street, S.; Zheng, J.; Pan, S. Single Ag Nanoparticle Spectroelectrochemistry via Dark-Field Scattering and Fluorescence Microscopies. *J. Phys. Chem. C* **2015**, *119*, 6760−6768.
(39) Pan, S.; Liu, J.; Hill, C. M. Observation of Local Redox Events at Individual Au Nanoparticles Using Electrogenerated Chemiluminescence Microscopy. *J. Phys. Chem. C* **2015**, *119*, 27095−27103.
(40) Wusimanjiang, Y.; Ma, Y.; Lee, M.; Pan, S. Single Gold Nanoparticle Electrode for Electrogenerated Chemiluminescence and Dark Field Scattering Spectroelectrochemistry. *Electrochim. Acta* **2018**, *269*, 291−298.
(41) Ma, Y.; Highsmith, A. L.; Hill, C. M.; Pan, S. Dark-Field Scattering Spectroelectrochemistry Analysis of Hydrazine Oxidation at Au Nanoparticle-Modified Transparent Electrodes. *J. Phys. Chem. C* **2018**, *122*, 18603−18614.
(42) González-García, J.; Gallud, F.; Iniesta, J.; Montiel, V.; Aldaz, A.; Lasia, A. Kinetics of Electrocrystallization of PbO_2 on Glassy Carbon Electrodes Partial Inhibition of the Progressive Three-Dimensional Nucleation and Growth. *J. Electrochem. Soc.* **2000**, *147*, 2969−2974.
(43) Hsu, H.-Y.; Ji, L.; Du, M.; Zhao, J.; Yu, E. T.; Bard, A. J. Optimization of PbI_2/$MAPbI_3$ Perovskite Composites by Scanning Electrochemical Microscopy. *J. Phys. Chem. C* **2016**, *120*, 19890−19895.
(44) Sultana, N.; Demarais, N. J.; Shevchenko, D.; Derrick, P. J. Laser Desorption/Ionization Mass Spectrometry of Perovskite Solar Cells: Identification of Interface Interactions and Degradation Reactions. *Sol. RRL* **2018**, *2*, 1800022−1800030.

https://dx.doi.org/10.1021/acs.jpcc.0c01536
J. Phys. Chem. C 2020, 124, 10659−10668